BIOCHEMISTRY

Decreased conformational stability in the oncogenic N92I mutant of Ras-related C3 botulinum toxin substrate 1

Yuki Toyama[1,2], Kenji Kontani[3], Toshiaki Katada[4], Ichio Shimada[1]*

Ras-related C3 botulinum toxin substrate 1 (Rac1) functions as a molecular switch by cycling between an inactive guanosine diphosphate (GDP)–bound state and an active guanosine triphosphate (GTP)–bound state. An oncogenic mutant of Rac1, an N92I mutant, strongly promotes cell proliferation and subsequent oncogenic activities by facilitating the intrinsic GDP dissociation in the inactive GDP-bound state. Here, we used solution nuclear magnetic resonance spectroscopy to investigate the activation mechanism of the N92I mutant. We found that the static structure of the GDP binding site is not markedly perturbed by the mutation, but the overall conformational stability decreases in the N92I mutant, which then facilitates GDP dissociation by lowering the activation energy for the dissociation reaction. On the basis of these results, we proposed the activation mechanism of the N92I mutant, in which the decreased conformational stability plays important roles in its activation process.

INTRODUCTION

Ras-related C3 botulinum toxin substrate 1 (Rac1) is a member of the Rho family of small guanine nucleotide-binding proteins (G proteins), which plays critical roles in the maintenance of cell morphology and cell migration (1, 2). Rac1 functions as a binary molecular switch by cycling between two distinct functional states depending on the bound nucleotide, an inactive guanosine diphosphate (GDP)–bound state and an active guanosine triphosphate (GTP)–bound state. The active GTP-bound Rac1 binds to different classes of proteins, including kinases, scaffold proteins, and enzymes, thus leading to the activation of downstream signaling pathways. The aberrant functions of Rac1 are closely related to diseases, especially cancer generation and progression. Recently, extensive sequencing analyses have revealed that gain-of-function mutations of Rac1 are frequently found in human cancers and that these mutations strongly promote cell proliferation and subsequent oncogenic activities. The oncogenic mutation, Pro[29] to Ser, was first identified from exome sequencing analyses of sun-exposed melanomas (3, 4), and subsequently, another mutation, Asn[92] to Ile, was found from deep sequencing analyses of the HT1080 human sarcoma cell line (5). Biochemical studies of these oncogenic mutant proteins have revealed that the intrinsic GDP dissociation reaction is accelerated in these mutants, and hence, they are maintained in the active GTP-bound state (5, 6).

Recently, we have investigated the activation mechanism of the oncogenic P29S mutant by using solution nuclear magnetic resonance (NMR) techniques (7). Our NMR results revealed that, in the P29S mutant, the preexisting conformational equilibrium in the switch 1 region (residues 30 to 38) is shifted toward the minor conformation that exhibits low affinity for Mg^{2+}, a cofactor that stabilizes the GDP binding, and that the increase in the Mg^{2+}-unbound state greatly facilitates the overall GDP dissociation in the P29S mutant. Whereas the

activation mechanism of the P29S mutant has been well characterized, less is known about the activation mechanism of another oncogenic mutant, the N92I mutant. Because the Asn[92] residue is distant from the switch 1 region, the activation mechanism of the N92I mutant is expected to be distinct from that of the P29S mutant. In the crystal structures of the wild-type GDP-bound Rac2 in the Rho–guanine nucleotide dissociation inhibitor (GDI)–bound state [Protein Data Bank (PDB) ID: 1DS6] and Rac1 in the uncomplexed state (PDB ID: 5N6O), the side chain of Asn[92] forms a hydrogen bond with the side chain of Asp[11] located on the phosphate-binding loop (P-loop; residues 10 to 17), which forms direct interactions with the bound GDP (fig. S1) (8, 9). From the modeled structure of the N92I mutant, predicted on the basis of the wild-type structure, an original proposal was that the N92I mutation results in a structural difference in the P-loop region, which then causes a decrease in the binding affinity for GDP and leads to the accelerated GDP dissociation (5). However, because of the lack of high-resolution structural information for the N92I mutant, the detailed mechanism has remained unclear.

Here, we investigated the activation mechanism of the Rac1 N92I oncogenic mutant by using solution NMR spectroscopy. We demonstrated that the P-loop structure is actually not markedly perturbed by the introduction of the N92I mutation. Instead, we found that the structure of the α3 helix is locally perturbed and that the overall conformational stability decreases in the mutant, which facilitates the GDP dissociation by lowering the activation energy for the dissociation reaction. We further revealed that the hydrogen bond interaction, formed between the Asp[11] and Trp[97] side chains in the wild type, determines the overall conformational stability and the GDP binding affinity and that this interaction is sterically blocked by the introduction of the N92I mutation. On the basis of these results, we proposed the activation mechanism of the N92I mutant, in which the decreased conformational stability plays important roles in its activation process.

[1]Graduate School of Pharmaceutical Sciences, The University of Tokyo, Hongo, Bunkyo-ku, Tokyo 113-0033, Japan. [2]Japan Biological Informatics Consortium (JBiC), Aomi, Koto-ku, Tokyo 135-0064, Japan. [3]Department of Biochemistry, Meiji Pharmaceutical University, Kiyose, Tokyo 204-8588, Japan. [4]Molecular Cell Biology Laboratory, Research Institute of Pharmaceutical Sciences, Faculty of Pharmacy, Musashino University, Tokyo 202-8585, Japan.
*Corresponding author. Email: shimada@iw-nmr.f.u-tokyo.ac.jp

RESULTS

The N92I mutant has a reduced affinity for GDP

First, we characterized the GDP dissociation rates in the presence of various concentrations of Mg^{2+}, which is known to be critical for

maintaining stable GDP binding (10). The GDP dissociation rates were measured by monitoring the reduction in the fluorescence intensity caused by the dissociation of preloaded 2′-(or-3′)-O-(N-methylanthraniloyl)–GDP (mant-GDP), in the presence of an excess amount of GTP. In the N92I mutant, the dissociation rates of mant-GDP were significantly faster than those of the wild type, in both the presence and absence of Mg^{2+}, and up to 30-fold faster than those of the wild type in the physiological range of Mg^{2+} concentration (0.2 to 1.2 mM) (Fig. 1A and table S1) (11). Whereas the apparent dissociation constant (K_d) of Mg^{2+} in the N92I mutant (26.6 ± 3.5 μM) was only threefold weaker than that of the wild type (8.9 ± 0.7 μM), the mant-GDP dissociation rate in the absence of Mg^{2+} was about 11-fold faster in the N92I mutant (Fig. 1B). These results indicate that the accelerated GDP dissociation in the N92I mutant is largely caused by the reduced binding affinity for GDP itself rather than the reduced binding affinity for Mg^{2+}. We note that this hyperactivation mechanism is in contrast to that of another oncogenic mutant, the P29S mutant. Recently, we revealed that the wild-type Rac1 exists in a conformational equilibrium between the major substate (A state) with high affinity for Mg^{2+} and the minor substate with low affinity for Mg^{2+} (B state), exchanging on the microsecond time scale (7). We showed that, in the P29S mutant, the equilibrium is shifted toward the B state and thus exhibits lower affinity for Mg^{2+}, which is responsible for the accelerated GDP dissociation under physiological conditions. In the case of the N92I mutant, this conformational equilibrium is not markedly different from that in the wild type, as supported by the results that the ^{13}C and ^{1}H relaxation dispersion (RD) profiles were not largely different from those observed in the wild type (fig. S2). These results support the hypothesis that the activation mechanism of the N92I mutant is distinct from that of the P29S mutant.

Structural differences in the α3 helix of the N92I mutant

To investigate the structural mechanisms underlying the reduced affinity for GDP in the N92I mutant, we prepared u-[^{2}H, ^{15}N]–labeled

Fig. 1. Mant-GDP dissociation rates of the wild type and the N92I mutant Rac1. (**A**) Mant-GDP dissociation rates of the wild type (left) and the N92I mutant (right). The data depicted as EDTA were measured in the presence of 1 mM EDTA. (**B**) Apparent K_d of Mg^{2+} of the wild type (left) and the N92I mutant (right). K_d values were calculated by using the equation, $k_{off,GDP}([Mg^{2+}]) = A \times K_d/([Mg^{2+}] + K_d) + B$, where A and B are constants. Each point reflects means ± SE of three independent experiments. The data for the wild type were originally reported in (7).

Rac1 samples and compared the ^{1}H-^{15}N transverse relaxation optimized spectroscopy (TROSY) spectra between the wild type and the N92I mutant (12). In all of the NMR experiments, we introduced the R66E mutation to suppress the self-association. We previously demonstrated that the introduction of the R66E mutation did not largely affect the apparent K_d for Mg^{2+} and that the chemical shift differences between the wild type and the R66E mutant were observed only for the residues that are in close vicinity to Arg^{66} (7). When we compared the NMR spectra between the wild type and the N92I mutant, significant chemical shift differences greater than the SD [0.15 parts per million (ppm)] were observed for the residues from the entire α3 helix, on which Asn^{92} is located, indicating that notable changes in the chemical environments occur on the α3 helix in the N92I mutant (Fig. 2). We also compared the secondary structure populations between the wild type and the N92I mutant, using the backbone chemical shifts with the δ2D software (13). We found that differences in the helix population greater than 2 SDs (0.054) were observed mainly in the residues forming the α3 helix (residues 91 to 96) and that relatively small differences were observed for the residues around the α4 helix as well (residues 145, 149, 150, and 151) (fig. S3). These results indicate that the structural differences between the wild type and the N92I mutant are highly localized to the region around the α3 helix and that these structural differences allosterically perturb the structure of the adjacent α4 helix.

Notably, the residues from the P-loop region showed smaller chemical shift differences up to 0.2 ppm than those observed in the α3 helix (Fig. 2), suggesting that the P-loop structure is not markedly perturbed by the introduction of the N92I mutation. To further characterize the differences in the P-loop structure, we measured nuclear Overhauser spectroscopy (NOESY) spectra and compared the results between the wild type and the N92I mutant. The cross peaks were observed between the same atomic pairs in the wild type and the N92I mutant, and the observed NOE patterns were compatible with the crystal structures of the Rac2-RhoGDI complex (PDB ID: 1DS6) and of the uncomplexed Rac1 (PDB ID: 5N6O; figs. S1 and S4, A and B) (8, 9). We further compared the backbone amide ^{1}H-^{15}N residual dipolar couplings (RDCs) between the wild type and the N92I mutant. The observed RDC patterns were not very different between them, and their values were compatible with the calculated RDCs obtained from the crystal structure (fig. S4C). We also found that the ^{31}P chemical shifts of the bound GDP were almost the same between the wild type and the N92I mutant, reflecting that the interactions formed between the bound GDP and the P-loop residues are not largely affected (fig. S4D). Collectively, these results indicate that neither the structure of the P-loop nor the interactions formed between the P-loop and the bound-GDP are markedly different between the wild type and the N92I mutant and that the local structural differences in the α3 helix are responsible for the increased GDP dissociation rate in the N92I mutant.

Decreased conformational stability in the N92I mutant

To characterize how the structural differences in the α3 helix affect the thermal stability and the GDP binding property, we first compared the thermal denaturation temperatures (T_m) between the wild type and the N92I mutant. The T_m values of the wild type and the N92I mutant were 64.8° and 53.6°C, respectively, showing that the conformational stability greatly decreases in the N92I mutant (Fig. 3A). We also measured the T_m value of another oncogenic mutant, the P29S mutant, and found that the T_m value of the P29S mutant (65.0°C) was
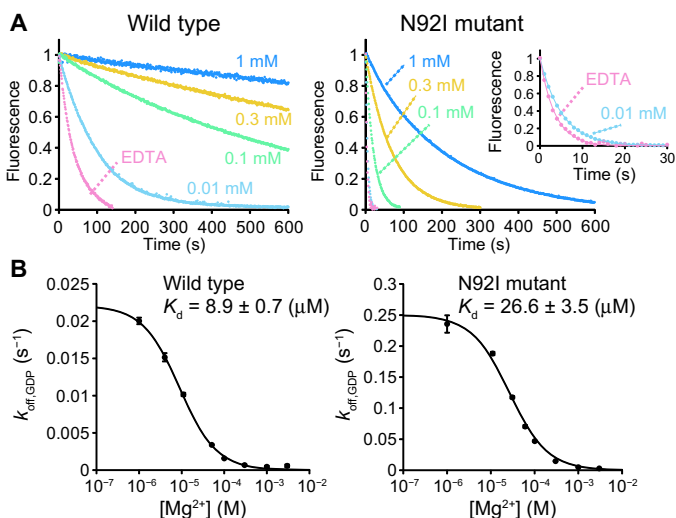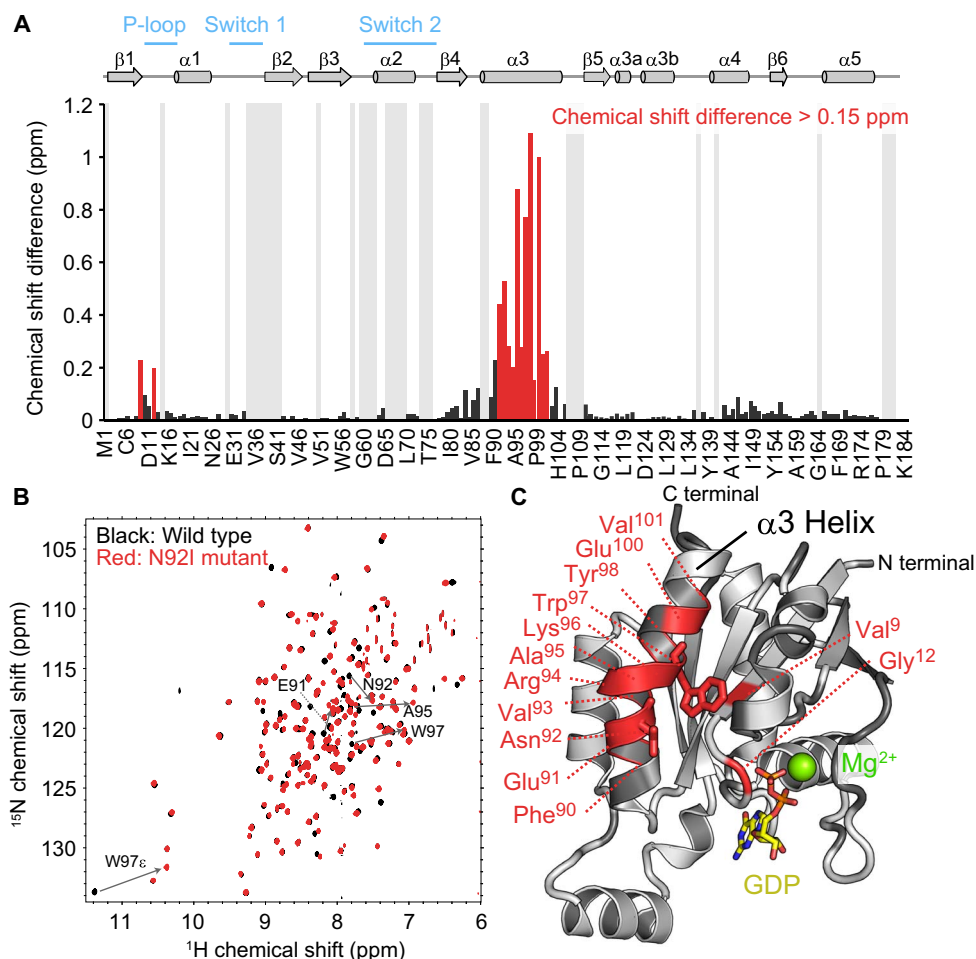
Fig. 2. Chemical shift differences between the wild type and the N92I mutant Rac1. (**A**) Plot of the normalized chemical shift differences between the wild type and the N92I mutant, $\Delta\delta$. $\Delta\delta$ is calculated by the equation, $\Delta\delta = \{(\Delta\delta_{1H})^2 + (\Delta\delta_{15N}/5)^2\}^{0.5}$. The residues with $\Delta\delta$ values larger than the SD (0.15 ppm) are colored red. (**B**) Overlay of the ^{1}H-^{15}N TROSY spectra of the wild type (black) and the N92I mutant (red), measured at 11.7 T (^{1}H frequency, 500 MHz) and 25°C. The signals with $\Delta\delta$ values larger than 0.4 ppm are labeled. (**C**) Mapping of the residues with $\Delta\delta$ values larger than 0.15 ppm on the structure of Rac1 (PDB ID: 1DS6) (8). The residues with no data are colored gray.

almost the same as that of the wild type, indicating that the decrease in thermal stability is the characteristic feature of the N92I mutant. We then quantitatively evaluated the difference in the activation free energy of unfolding by measuring the unfolding rate constants in the presence of various concentrations of a denaturant, guanidine hydrochloride (14). By linear extrapolation, we found that the unfolding rate constant of the N92I mutant is about 10.5-fold faster than that of the wild type in the absence of guanidine hydrochloride, which corresponds to a difference in the activation free energy of unfolding, $\Delta\Delta G^{\ddagger}_{\text{unfold}}$, of 1.39 kcal/mol (Fig. 3B). Notably, this free energy difference was consistent with the difference in the activation free energy of GDP dissociation, $\Delta\Delta G^{\ddagger}_{\text{GDP,off}}$, of 1.22 kcal/mol. This $\Delta\Delta G^{\ddagger}_{\text{GDP,off}}$ value was calculated from the differences in the mant-GDP dissociation rates between the wild type and the N92I mutant in the absence of Mg^{2+} to estimate the energetic contributions to the GDP binding free energy and not to the Mg^{2+} binding free energy. These results strongly suggest that the Rac1 unfolding and the GDP dissociation events share part of their energetic landscapes and that the decreased conformational stability lowers the activation energy barrier for the GDP dissociation reaction. In these energetic land-

scapes, note that the conformational substates with different affinities for Mg^{2+} (states A and B), which are exchanging on the microsecond time scale, are not markedly altered by the introduction of the N92I mutation (Fig. 3C) (7). We also found that the mant-GDP dissociation rate greatly increased in the presence of low concentrations of guanidine hydrochloride, which facilitates the unfolding of wild-type Rac1 (fig. S5).

The α3 helix–P-loop interaction determines the conformational stability

To identify the key structural elements that play critical roles in determining the overall conformational stability and the GDP binding affinity, we analyzed the temperature-dependent changes in the amide NH and Trp ε-NH chemical shifts, which not only define the intramolecular hydrogen bonding but also serve as sensitive reporters for both the local and global structural stabilities of proteins (15–18). We measured ^{1}H-^{15}N TROSY spectra at 20° to 35°C and calculated the ^{1}H chemical shift changes per degree of temperature, hereafter referred to as the temperature coefficient $\Delta\delta/\Delta T$. We then compared the $\Delta\delta/\Delta T$ values of the wild type with those of the N92I mutant (Fig. 4A and
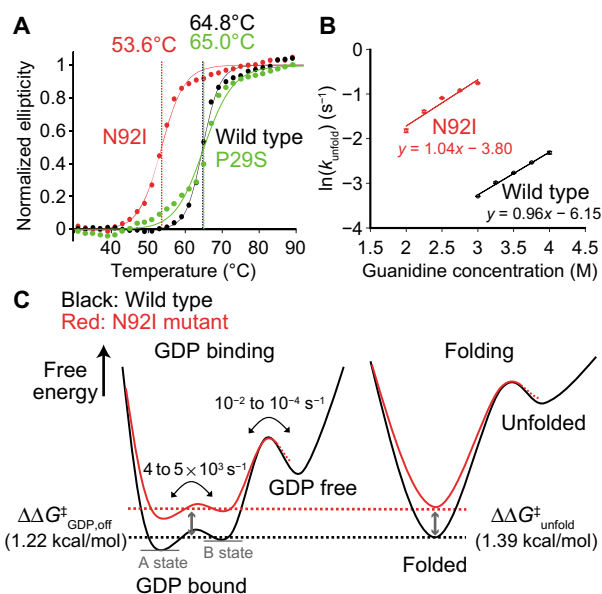
Fig. 3. Conformational stability of Rac1. (**A**) Thermal denaturation curves of the wild type (black), the P29S mutant (green), and the N92I mutant (red), based on circular dichroism measurements observing the molar ellipticity at 222 nm. (**B**) Plots of the unfolding rates of the wild type (black) and the N92I mutant (red), measured in the presence of various concentrations of guanidine hydrochloride. (**C**) Schematic representations of the free energy landscape of the GDP binding reaction (left) and the folding reaction (right). The free energy landscapes of the wild type and the N92I mutant are colored black and red, respectively. The A and B states are the previously identified substates in the GDP-bound state, which differ in the affinity for Mg^{2+} (7).

fig. S6). The $\Delta\delta/\Delta T$ values of the wild type and the mutants were very similar for most of the residues, indicating that the structural reorganizations in the N92I mutant are restricted to local regions. The notable decrease in $\Delta\delta/\Delta T$, up to −5.3 parts per billion/°C, was observed in the side chain of Trp[97] in the N92I mutant, indicating that the hydrogen bond interaction involving the side chain of Trp[97] is lost in the mutant. Small but significant differences in $\Delta\delta/\Delta T$ were also observed in the main chains of Ala[95], Lys[96], and Trp[97], reflecting the stretching or shortening of hydrogen bonds caused by the local structural differences of the α3 helix. In the crystal structures (PDB IDs: 1DS6 and 5N6O), the side-chain ε-NH of Trp[97], located on the α3 helix, forms a hydrogen bond with the carboxyl oxygen of Asp[11], located on the P-loop region (Fig. 4B and fig. S1). To test whether the loss of the hydrogen bond formed between the Asp[11] and Trp[97] side chains is responsible for the accelerated GDP dissociation, we prepared a W97A mutant protein. We confirmed that the chemical shift differences between the wild type and the W97A mutant were mainly observed for the residues in the close vicinity of Trp[97] and that the overall structure is minimally affected by the introduction of the W97A mutation (fig. S7, A to C). Notably, when we measured its mant-GDP dissociation rate, the mant-GDP dissociation rate markedly increased in the W97A mutant, as compared to the mutants of other residues on the α3 helix (Fig. 4, B and C, and table S2). In addition, the T_m value of the W97A mutant was 50.0°C, as compared to 64.8°C in the wild type, showing that the conformational stability greatly decreased in the W97A mutant (fig. S7D). These results indicate that the side chain of Trp[97] is a critical factor that determines the stability of GDP binding. As stated above, the side chain of Trp[97] participates in the hydrogen bond with the side chain of Asp[11]. Thus, these results strongly suggest that the loss of this hydrogen bond in the
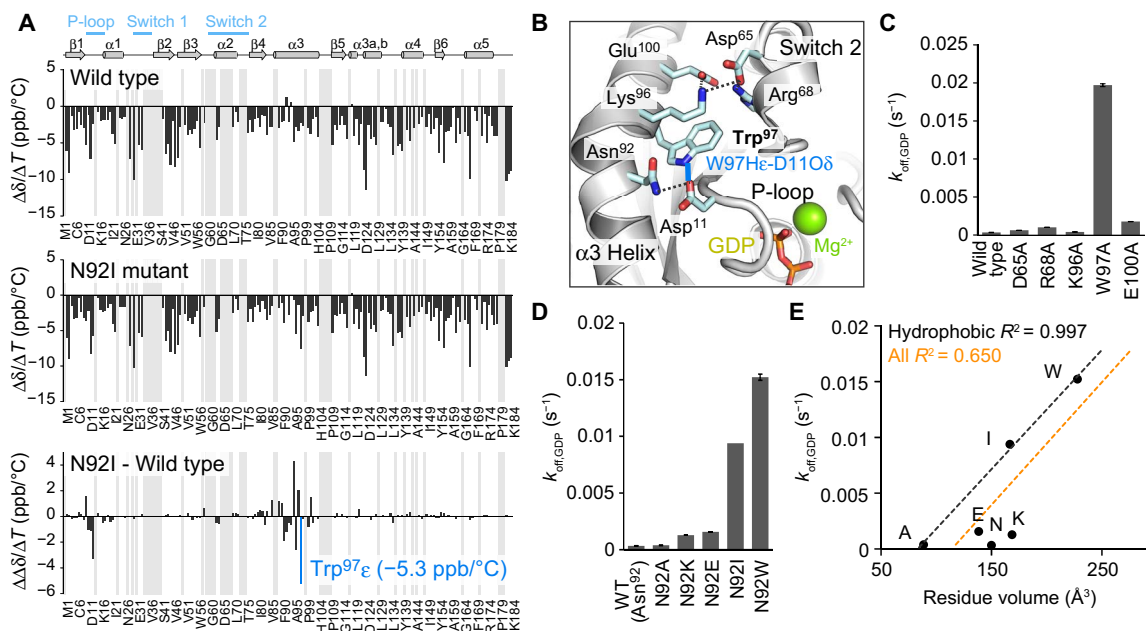

Fig. 4. Experimental identification of the key hydrogen bond interaction that determines the conformational stability. (**A**) Plots of the amide and Trp ε-NH ^1H temperature coefficients, $\Delta\delta/\Delta T$, of the wild type (top) and the N92I mutant (middle). The plot of the differences in $\Delta\delta/\Delta T$ between the wild type and the N92I mutant is also shown (bottom). ppb, parts per billion. (**B**) Close-up view of the interactions formed between the α3 helix and the switch 2 region (PDB ID: 1DS6) (8). (**C**) Mant-GDP dissociation rates of the mutants of the residues that participate in the interaction formed between the α3 helix and the switch 2 region. (**D**) Mant-GDP dissociation rates of the Asn[92] mutants. (**E**) Correlation plots of the mant-GDP dissociation rates of the Asn[92] mutants versus the side-chain volumes (40).

N92I mutant is responsible for the decreased overall conformational stability in the mutant.

We also investigated the structural mechanism for the loss of the Asp[11]-Trp[97] hydrogen bond in the N92I mutant by replacing Asn[92] with other amino acids with different properties (Fig. 4D and table S3). When we mutated Asn[92] to charged amino acids, the mant-GDP dissociation rates changed slightly. In contrast, when we replaced Asn[92] with hydrophobic amino acids with different steric bulkiness, the mant-GDP dissociation rate increased as the side-chain volume increased, indicating that the formation of the Asp[11]-Trp[97] hydrogen bond is hampered by the steric hindrance with the side chain of the residue at position 92 (Fig. 4E). This proposed mechanism is also supported from the molecular dynamics simulations of Rac1 (Fig. 5). During the 50-ns simulation using the wild-type structure, the hydrogen bond formed between the Trp[97] ε-NH and the carboxyl oxygen of Asp[11] remained stable. In contrast, when we conducted the simulations using the N92I mutant structure, the distance between the Trp[97] ε-NH and the carboxyl oxygen of Asp[11] was mainly distributed around 4 Å, indicating that the hydrogen bond is not stably formed between these atoms. The trajectory of the N92I mutant revealed that the Asp[11] side-chain conformer exclusively adopts the trans conformation because of steric hindrance with the γ2 methyl group of Ile[92]. In the trans conformation, the carboxylic group of Asp[11] is further away from the side chain of Trp[97], and thereby, the hydrogen bond cannot be formed between them.

DISCUSSION

In this study, we investigated the activation mechanism of the oncogenic N92I mutant of Rac1. We found that, whereas the structure of the P-loop is not markedly perturbed, the structure of the α3 helix is locally perturbed, and the overall conformational stability decreases in the N92I mutant. We also revealed that the hydrogen bond interaction formed between the Asp[11] and Trp[97] side chains determines the overall conformational stability and that the replacement of Asn[92] with Ile sterically blocks this interaction and thus substantially decreases the overall conformational stability. Considering that both the decrease in the conformational stability and the loss of the hydrogen bond interaction in the N92I mutant were observed in the GDP-bound state, we propose that the decreased conformational stability increases the ground-state free energy of the GDP-bound state, and hence, lowers the activation energy along the GDP dissociation reaction coordinate, leading to faster GDP dissociation in the mutant (Fig. 6). This mechanism is consistent with the observation that, in the structure of the GDP-bound Rac1, the bound GDP forms an extensive hydrogen bond network that stabilizes the ternary complex and the
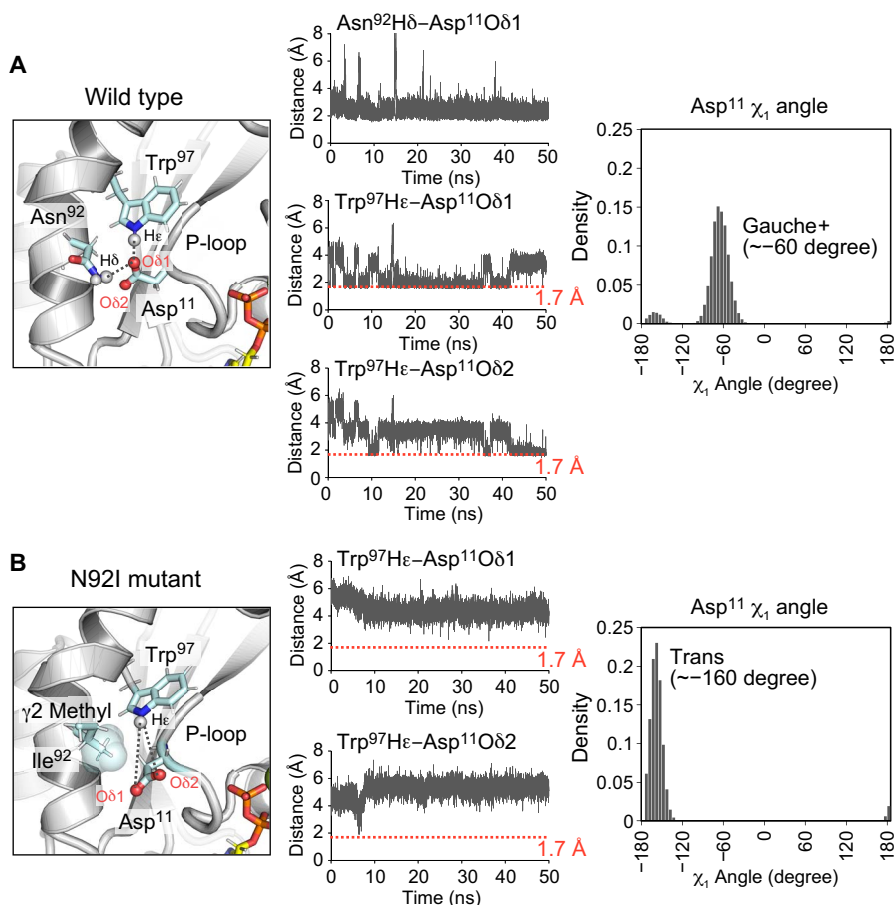

Fig. 5. Molecular dynamics simulations of Rac1. (**A**) Close-up view of the wild-type Rac1 structure obtained after the 50-ns simulation (left). Plots of the distances between Asn[92]Hδ-Asp[11]Oδ1, Trp[97]Hε-Asp[11]Oδ1, and Trp[97]Hε-Asp[11]Oδ2 (center). Histogram of the distribution of Asp[11] side-chain χ₁ angles (right). (**B**) Close-up view of the N92I mutant Rac1 structure obtained after the 50-ns simulation (left). Plots of the distances between Trp[97]Hε-Asp[11]Oδ1 and Trp[97]Hε-Asp[11]Oδ2 (center). Histogram of the distribution of Asp[11] side-chain χ₁ angles (right).
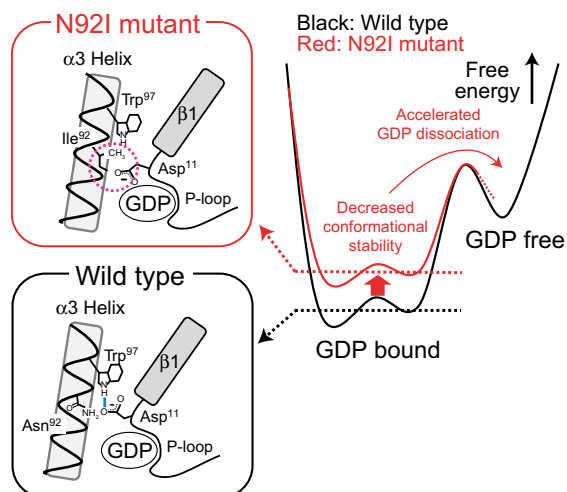
Fig. 6. Schematic illustration of the decreased conformational stability in the N92I mutant and its activation mechanism. In the wild type (black), a hydrogen bond interaction (blue line) is formed between Asp[11] and Trp[97]. In the N92I mutant (red), the side chain of Ile[92] sterically blocks the hydrogen bond interaction (magenta circle). The loss of this hydrogen bond in the N92I mutant increases the GDP-bound ground-state energy and hence accelerates the GDP dissociation by lowering the activation energy along the GDP dissociation reaction coordinate.

dissociation of GDP is expected to involve the relaxation of the Rac1 structure (8). Several lines of evidence have shown that the nucleotide-free states of G proteins represent partially unfolded structures and that the GDP dissociation occurs via partially unfolded intermediates (19–21). We note that our conclusion is in contrast to the originally proposed mechanism, in which GDP binding is affected in the N92I mutant through an effect on the P-loop structure by the loss of the hydrogen bond interaction formed between the side chains of Asp[11] and Asn[92] in the wild type (5). We presume that the interaction formed between Asp[11] and Asn[92] does not greatly contribute to maintaining the P-loop structure in the wild type because the simple loss of this interaction in the N92A mutant hardly affected the mant-GDP dissociation rate (Fig. 4D) and that the P-loop structure is highly preserved in the structural model of the N92I mutant despite the absence of this interaction (Fig. 5). The decrease in the conformational stability would also affect the GTP dissociation rate; however, the difference in the GTP dissociation rate is expected to be smaller than that observed in the GDP dissociation rate. This is because the GTP dissociation rate is about 25-fold slower than the GDP dissociation rate (22) and because the activation energy barrier is higher for the GTP dissociation reaction than that for the GDP dissociation. This notion is fully supported by the previous observation that the GTP dissociation rates were not markedly different between the wild type and the N92I mutant (5).

Our results have established that the local structural differences around the α3 helix, which is distant from the GDP binding pocket, markedly alter the binding affinity for GDP by affecting its overall conformational stability. This mechanism indicates that, in the N92I mutant, the acceleration of the GDP dissociation and the subsequent stabilization of the GTP-bound state are achieved in an allosteric manner without perturbing the structures and dynamics of the P-loop and the switch regions. Because the interactions with downstream effector proteins occur exclusively on the switch regions, and not on the α3 helix (23–26), the interactions with the effector proteins

are expected to be highly preserved in the N92I mutant. This property would explain the strong oncogenic activity of the N92I mutant, as previously observed in cellular experiments (5).

Recently, a growing amount of evidence has shown that the formation of unfolded states plays important roles in a wide variety of biological processes, such as ligand binding and enzymatic reactions (27, 28). Our findings have established that the decrease in the conformational stability can be induced by disease-related mutations and that the aberrant functions of proteins caused by the decreased stability actually play critical roles in pathogenic processes. Therefore, the present study may open the possibility of designing drugs that can modulate the activities of proteins by regulating their conformational stability.

METHODS

Protein expression and purification

The Rac1 protein (human Rac1, residues 1 to 184) was expressed in *Escherichia coli* cells as a glutathione-*S*-transferase (GST) fusion protein, as described previously (5, 7). To suppress the self-association into a dimer at concentrations more than 10^2 μM, we used an R66E mutant in all of the NMR experiments (7). The Rac1 mutants were constructed with the QuikChange II Site-Directed Mutagenesis Kit (Agilent Technologies). *E. coli* BL21-CodonPlus(DE3)-RP cells (Agilent Technologies), transformed with the pGEX-6P-1 plasmid encoding Rac1, were grown at 37°C in LB media for preparing nonlabeled samples or in deuterated M9 media for preparing isotopically labeled NMR samples. When ^{15}N labeling was required, ^{15}NH$_4$Cl was used as the sole nitrogen source. For the selective ^{13}CH$_3$ labeling of methyl groups, [3-^{13}C, 2-^{2}H]-L-alanine (200 mg/liter, for Alaβ), [methyl-^{13}C, 3,3-^{2}H$_2$]-α-ketobutyric acid [50 mg/liter, for Ileδ1; Cambridge Isotope Laboratories (CIL)], [3-methyl-^{13}C, 3,4,4,4-^{2}H$_4$]-α-ketoisovaleric acid (80 mg/liter, for Leuδ1, Leuδ2, Valγ1, and Valγ2; CIL), [methyl-^{13}C]-L-methionine (100 mg/liter, for Metε; CIL), and [2,2,3,3-^{2}H$_4$]-succinic acid (2.5 g/liter; CIL) were added 1 hour before the induction. The production of the Rac1 protein was induced with 0.1 mM isopropyl β-D-1-thiogalactopyranoside at 20°C for 16 hours. The protein was purified to homogeneity by chromatography on Glutathione Sepharose 4B resin (GE). After cleavage of the GST-tag with PreScission protease (GE), the protein was further purified by size exclusion chromatography using the HiLoad 26/60 Superdex 75 pg (GE) in buffer containing 20 mM tris (pH 7.5), 150 mM NaCl, 5 mM MgCl$_2$, and 1 mM dithiothreitol (DTT). To observe the amide signals, the purified protein was incubated at 37°C for 36 hours in MgCl$_2$-free buffer to exchange the amide hydrogen atom from ^{2}H to ^{1}H. NMR samples were prepared by changing the buffer to 20 mM Hepes-NaOH (pH 7.0), 0.5 mM GDP, 5 mM MgCl$_2$, and 5 mM DTT by sequential dilution and concentration with an Amicon Ultra Centrifugal Filter Unit, NMWL (nominal molecular weight limit) 10 kDa (Merck Millipore).

Mant-GDP dissociation rate measurements

The dissociation rate of mant-GDP was measured by monitoring the reduction in the fluorescence intensity due to the dissociation of mant-GDP preloaded in Rac1 (10). The purified Rac1 protein (20 μM) was incubated at 30°C for 30 min in buffer containing 50 mM tris-HCl (pH 7.5), 100 mM NaCl, 0.1 mM MgCl$_2$, 1 mM DTT, and 50 μM mant-GDP (Invitrogen). The dissociation reaction was initiated by a 100-fold dilution in buffer containing 200 μM GTP and various concentrations of MgCl$_2$. The excitation and emission wavelengths were set to

355 and 448 nm, respectively, with slit widths of 5 nm. The measurements were performed at 30°C. The difference in the activation free energy was calculated according to $\Delta\Delta G^{\ddagger}_{\text{GDP,off}} = -RT\ln(k_{\text{off,WT}}/k_{\text{off,N92I}})$, in which R denotes the gas constant and T represents the absolute temperature.

Circular dichroism measurements

The T_m values were obtained from the temperature-dependent changes in the molar ellipticity. The purified Rac1 protein (10 μM) was prepared in buffer containing 50 mM tris-HCl (pH 7.5), 100 mM NaCl, 5 mM MgCl₂, 10 μM GDP, and 1 mM DTT, and its molar ellipticity at 222 nm was monitored. The temperature was changed from 30° to 90°C in 1.5°C increments, with 30 s of equilibration time. The T_m values were obtained by fitting the temperature-dependent changes in molar ellipticity by using the Gibbs-Helmholtz equation (29).

Measurements of unfolding rates

The unfolding rate of Rac1 was measured by monitoring the reduction in the tryptophan fluorescence caused by protein unfolding (14). The purified Rac1 protein (1 μM) was prepared in buffer containing 50 mM tris-HCl (pH 7.5), 100 mM NaCl, 5 mM MgCl₂, 5 μM GDP, and 1 mM DTT. Then, the protein solution was rapidly mixed with an equivalent volume of buffer containing various concentrations of guanidine hydrochloride, and the time-dependent changes in the fluorescence were monitored. The unfolding rate under native conditions was determined by linear extrapolation to 0 M guanidine hydrochloride. The excitation and emission wavelengths were set to 281 and 340 nm, respectively, with slit widths of 5 nm. The measurements were performed at 25°C. The difference in the activation free energy was calculated according to $\Delta\Delta G^{\ddagger}_{\text{unfold}} = -RT\ln(k_{\text{unfold,WT}}/k_{\text{unfold,N92I}})$, in which R denotes the gas constant and T represents the absolute temperature.

NMR analyses

All ¹H-detected experiments were performed on Bruker AVANCE 500, 600, or 800 spectrometers equipped with cryogenic probes. ³¹P-detected experiments were performed on a Bruker AVANCE 400 spectrometer equipped with a BBFO probe. All spectra were processed by the Bruker TopSpin 2.1 or 3.1 software, and the data were analyzed using Sparky (T. D. Goddard and D. G. Kneller, Sparky 3, University of California, San Francisco, CA). Backbone resonance and side-chain methyl resonance assignments were obtained by combining out-and-back type triple-resonance experiments (30), NOE analyses based on the crystal structure, and mutagenesis approaches.

[¹H-¹H] NOESY-[¹⁵N-¹H]-TROSY spectra were obtained using u-[²H, ¹⁵N] Rac1 samples at 25°C with a Bruker AVANCE 600 spectrometer. The mixing time was set to 200 ms.

The ¹H-¹⁵N RDCs were obtained from the difference in the ¹⁵N-¹H J-coupling constants in aligned (pentaethylene glycol monododecyl ether/hexanol) and isotropic media. The J-coupling constants were measured from the differences between the TROSY and heteronuclear single-quantum coherence peak positions. The measurements were performed at 20°C with a Bruker AVANCE 600 spectrometer, using u-[²H, ¹⁵N] Rac1 samples. The alignment tensors and the calculated RDCs were obtained by singular value decomposition with the dipolar coupling computation server developed by the Ad Bax group (National Institutes of Health) (https://spin.niddk.nih.gov/bax/nmrserver/dc/svd.html) by using the coordinates of the Rac1 structure modeled from the crystal structure of the Rac2-RhoGDI

complex (PDB ID: 1DS6). In these analyses, the region with structural changes upon the binding of RhoGDI (residues 34 to 42) was not used.

To obtain the backbone ¹H (amide NH), ¹³C (Cα, Cβ, and CO), and ¹⁵N (amide N) chemical shifts for δ2D analyses (13), we prepared u-[¹³C, ¹⁵N] Rac1 samples and conducted triple-resonance experiments at 35°C (for the N92I mutant) or 40°C (for the wild type) with a Bruker AVANCE 500 spectrometer.

The ¹³C single-quantum (SQ) and ¹H triple-quantum (3Q) Carr-Purcell-Meiboom-Gill (CPMG) RD analyses were recorded at 25°C with Bruker AVANCE 600 and 800 spectrometers, using {u-[²H, ¹⁵N]; Alaβ, Ileδ1, Metε-[¹³CH₃], Leu, and Val-[¹³CH₃, ¹²C²H₃]} Rac1 samples (31, 32). The constant-time CPMG relaxation period T was set to 20 ms for the ¹³C SQ experiments and 5 ms for the ¹H 3Q experiments. The ν_{CPMG} values were varied between 50 and 1500 Hz for ¹³C SQ and between 200 and 3000 Hz for ¹H 3Q RD experiments. The values of the effective relaxation rates measured in the presence of a ν_{CPMG} Hz CPMG pulse train, $R_{2,\text{eff}}(\nu_{\text{CPMG}})$, were calculated using Eq. 1, where $I(\nu_{\text{CPMG}})$ and $I(0)$ represent the peak intensities with and without the relaxation period T, respectively.

$$R_{2,\text{eff}}(\nu_{\text{CPMG}}) = -\frac{1}{T}\ln\left\{\frac{I(\nu_{\text{CPMG}})}{I(0)}\right\} \qquad (1)$$

For residue-specific fitting, the ¹³C SQ and ¹H 3Q RD curves obtained with two static magnetic fields were simultaneously fitted to the Luz-Meiboom equation (Eq. 2) (33), where Φ_X (X = ¹³C or ¹H) denotes the dispersion amplitude parameter, $R_{2,0}$ denotes the intrinsic transverse relaxation rate, k_{ex} denotes the exchange rate, $\Delta\omega_X$ (X = ¹³C or ¹H) denotes the chemical shift difference, and p_B denotes the B state population (7)

$$R_{2,\text{eff}} = R_{2,0} + \frac{\Phi_X}{k_{\text{ex}}}\left(1 - \frac{4\nu_{\text{CPMG}}}{k_{\text{ex}}}\tanh\left(\frac{k_{\text{ex}}}{4\nu_{\text{CPMG}}}\right)\right)$$
$$\Phi_C = p_B(1-p_B)\Delta\omega_C^2$$
$$\Phi_H = p_B(1-p_B)(3\Delta\omega_H)^2 \qquad (2)$$

Backbone amide NH and Trp ε-NH ¹H temperature coefficients were calculated from the ¹H-¹⁵N TROSY spectra obtained at 293, 298, 303, and 308 K with a Bruker AVANCE 500 spectrometer, using u-[²H, ¹⁵N] Rac1 samples.

Molecular dynamics simulations

The all-atom model of Rac1 was constructed with CHARMM-GUI (34), using the crystal structure of the Rac2-RhoGDI complex (PDB ID: 1DS6), on the basis of our previous result that this structure well represents the ground-state structure of GDP-bound Rac1 in the uncomplexed state (7, 8). The Rac2 sequence was converted to that of Rac1 with or without the N92I mutation, and the structure including the bound GDP and Mg²⁺ was solvated in a periodic water box with a size of 74 Å by 74 Å by 74 Å, using TIP3P water molecules. The system was then neutralized with about 150 mM KCl. Molecular dynamics simulations were performed using the NAMD2.12 software (35) and the CHARMM36 parameter set (36). A cutoff distance of 12 Å was used for the van der Waals and short-range electrostatic interactions, and the long-range electrostatic interactions

were computed with the particle mesh Ewald method (*37*). Bonds containing hydrogen atoms were restrained with the SHAKE algorithm (*38*). Bonded and short-range electrostatic interactions were computed every 2 fs, and long-range electrostatic interactions were computed every 4 fs. The system was first energy-minimized for 500 steps and then equilibrated under isothermal-isobaric (NPT) conditions for 5 ns at 1 atm and 310 K. The production simulations were performed for 50 ns at 1 atm and 310 K. The trajectories were analyzed using the Visual Molecular Dynamics 1.9.3 software (*39*).

SUPPLEMENTARY MATERIALS

Supplementary material for this article is available at http://advances.sciencemag.org/cgi/content/full/5/8/eaax1595/DC1

Table S1. MANT-GDP dissociation rates of the wild type and the N92I mutant in the presence of various concentrations of Mg^{2+}.

Table S2. MANT-GDP dissociation rates of the mutants of the residues from the α3 helix and the switch 2 region.

Table S3. MANT-GDP dissociation rates of the mutants of Asn^{92}.

Fig. S1. Comparisons of the structures of Rac between the RhoGDI-bound state and the uncomplexed state.

Fig. S2. Microsecond-order conformational exchange processes in the wild type and the N92I mutant.

Fig. S3. Secondary structure populations of the wild type and the N92I mutant.

Fig. S4. Structural characterizations of the P-loop.

Fig. S5. Mant-GDP dissociation rates in the presence of guanidine hydrochloride.

Fig. S6. Temperature-dependent changes in the ^1H-^{15}N TROSY spectra.

Fig. S7. Characterizations of the structure and conformational stability of the W97A mutant.

REFERENCES AND NOTES

1. Y. Takai, T. Sasaki, T. Matozaki, Small GTP-binding proteins. *Physiol. Rev.* **81**, 153–208 (2001).
2. A. B. Jaffe, A. Hall, Rho GTPases: Biochemistry and biology. *Annu. Rev. Cell Dev. Biol.* **21**, 247–269 (2005).
3. E. Hodis, I. R. Watson, G. V. Kryukov, S. T. Arold, M. Imielinski, J.-P. Theurillat, E. Nickerson, D. Auclair, L. Li, C. Place, D. DiCara, A. H. Ramos, M. S. Lawrence, K. Cibulskis, A. Sivachenko, D. Voet, G. Saksena, N. Stransky, R. C. Onofrio, W. Winckler, K. Ardlie, N. Wagle, J. Wargo, K. Chong, D. L. Morton, K. Stemke-Hale, G. Chen, M. Noble, M. Meyerson, J. E. Ladbury, M. A. Davies, J. E. Gershenwald, S. N. Wagner, D. S. B. Hoon, D. Schadendorf, E. S. Lander, S. B. Gabriel, G. Getz, L. A. Garraway, L. Chin, A landscape of driver mutations in melanoma. *Cell* **150**, 251–263 (2012).
4. M. Krauthammer, Y. Kong, B. H. Ha, P. Evans, A. Bacchiocchi, J. P. McCusker, E. Cheng, M. J. Davis, G. Goh, M. Choi, S. Ariyan, D. Narayan, K. Dutton-Regester, A. Capatana, E. C. Holman, M. Bosenberg, M. Sznol, H. M. Kluger, D. E. Brash, D. F. Stern, M. A. Materin, R. S. Lo, S. Mane, S. Ma, K. K. Kidd, N. K. Hayward, R. P. Lifton, J. Schlessinger, T. J. Boggon, R. Halaban, Exome sequencing identifies recurrent somatic *RAC1* mutations in melanoma. *Nat. Genet.* **44**, 1006–1014 (2012).
5. M. Kawazu, T. Ueno, K. Kontani, Y. Ogita, M. Ando, K. Fukumura, A. Yamato, M. Soda, K. Takeuchi, Y. Miki, H. Yamaguchi, T. Yasuda, T. Naoe, Y. Yamashita, T. Katada, Y. L. Choi, H. Mano, Transforming mutations of RAC guanosine triphosphatases in human cancers. *Proc. Natl. Acad. Sci. U.S.A.* **110**, 3029–3034 (2013).
6. M. J. Davis, B. H. Ha, E. C. Holman, R. Halaban, J. Schlessinger, T. J. Boggon, RAC1^{P29S} is a spontaneously activating cancer-associated GTPase. *Proc. Natl. Acad. Sci. U.S.A.* **110**, 912–917 (2013).
7. Y. Toyama, K. Kontani, T. Katada, I. Shimada, Conformational landscape alternations promote oncogenic activities of Ras-related C3 botulinum toxin substrate 1 as revealed by NMR. *Sci. Adv.* **5**, eaav8945 (2019).
8. K. Scheffzek, I. Stephan, O. N. Jensen, D. Illenberger, P. Gierschik, The Rac–RhoGDI complex and the structural basis for the regulation of Rho proteins by RhoGDI. *Nat. Struct. Biol.* **7**, 122–126 (2000).
9. Y. Ferrandez, W. Zhang, F. Peurois, A. Akendengué, A. Blangy, M. Zeghouf, J. Cherfils, Allosteric inhibition of the guanine nucleotide exchange factor DOCK5 by a small molecule. *Sci. Rep.* **7**, 14409 (2017).
10. B. Zhang, Y. Zhang, Z.-x. Wang, Y. Zheng, The role of Mg^{2+} cofactor in the guanine nucleotide exchange and GTP hydrolysis reactions of Rho family GTP-binding proteins. *J. Biol. Chem.* **275**, 25299–25307 (2000).
11. R. E. London, Methods for measurement of intracellular magnesium:NMR and fluorescence. *Annu. Rev. Physiol.* **53**, 241–258 (1991).
12. K. Pervushin, R. Riek, G. Wider, K. Wüthrich, Attenuated T_2 relaxation by mutual cancellation of dipole–dipole coupling and chemical shift anisotropy indicates an avenue to NMR structures of very large biological macromolecules in solution. *Proc. Natl. Acad. Sci. U.S.A.* **94**, 12366–12371 (1997).
13. C. Camilloni, A. De Simone, W. F. Vranken, M. Vendruscolo, Determination of secondary structure populations in disordered states of proteins using nuclear magnetic resonance chemical shifts. *Biochemistry* **51**, 2224–2231 (2012).
14. A. K. Gardino, J. Villali, A. Kivenson, M. Lei, C. F. Liu, P. Steindel, E. Z. Eisenmesser, W. Labeikovsky, M. Wolf-Watz, M. W. Clarkson, D. Kern, Transient non-native hydrogen bonds promote activation of a signaling protein. *Cell* **139**, 1109–1118 (2009).
15. T. Cierpicki, J. Otlewski, Amide proton temperature coefficients as hydrogen bond indicators in proteins. *J. Biomol. NMR* **21**, 249–261 (2001).
16. J. H. Tomlinson, M. P. Williamson, Amide temperature coefficients in the protein G B1 domain. *J. Biomol. NMR* **52**, 57–64 (2012).
17. J. Hong, Q. Jing, L. Yao, The protein amide $^1H^N$ chemical shift temperature coefficient reflects thermal expansion of the N–H⋯O=C hydrogen bond. *J. Biomol. NMR* **55**, 71–78 (2013).
18. C. M. Doyle, J. A. Rumfeldt, H. R. Broom, A. Sekhar, L. E. Kay, E. M. Meiering, Concurrent increases and decreases in local stability and conformational heterogeneity in Cu, Zn superoxide dismutase variants revealed by temperature-dependence of amide chemical shifts. *Biochemistry* **55**, 1346–1361 (2016).
19. J. Zhang, C. R. Matthews, Ligand binding is the principal determinant of stability for the p21^{H-ras} protein. *Biochemistry* **37**, 14881–14890 (1998).
20. J. Zhang, C. R. Matthews, The role of ligand binding in the kinetic folding mechanism of human p21^{H-ras} protein. *Biochemistry* **37**, 14891–14899 (1998).
21. S. K. Andhirka, R. Vignesh, G. K. Aradhyam, The nucleotide-free state of heterotrimeric G proteins α-subunit adopts a highly stable conformation. *FEBS J.* **284**, 2464–2481 (2017).
22. L. Ménard, E. Tomhave, P. J. Casey, R. J. Uhing, R. Snyderman, J. R. Didsbury, Rac1, a low-molecular-mass GTP-binding-protein with high intrinsic GTPase activity and distinct biochemical properties. *Eur. J. Biochem.* **206**, 537–546 (1992).
23. K. Lapouge, S. J. M. Smith, P. A. Walker, S. J. Gamblin, S. J. Smerdon, K. Rittinger, Structure of the TPR domain of p67^{phox} in complex with Rac·GTP. *Mol. Cell* **6**, 899–907 (2000).
24. R. Dvorsky, M. R. Ahmadian, Always look on the bright site of Rho: Structural implications for a conserved intermolecular interface. *EMBO Rep.* **5**, 1130–1136 (2004).
25. M. R. Jezyk, J. T. Snyder, S. Gershberg, D. K. Worthylake, T. K. Harden, J. Sondek, Crystal structure of Rac1 bound to its effector phospholipase C-β2. *Nat. Struct. Mol. Biol.* **13**, 1135–1140 (2006).
26. T. D. Bunney, O. Opaleye, S. M. Roe, P. Vatter, R. W. Baxendale, C. Walliser, K. L. Everett, M. B. Josephs, C. Christow, F. Rodrigues-Lima, P. Gierschik, L. H. Pearl, M. Katan, Structural insights into formation of an active signaling complex between Rac and phospholipase C gamma 2. *Mol. Cell* **34**, 223–233 (2009).
27. D. M. Mitrea, R. W. Kriwacki, Regulated unfolding of proteins in signaling. *FEBS Lett.* **587**, 1081–1088 (2013).
28. H. N. Motlagh, J. O. Wrabl, J. Li, V. J. Hilser, The ensemble nature of allostery. *Nature* **508**, 331–339 (2014).
29. N. J. Greenfield, Using circular dichroism collected as a function of temperature to determine the thermodynamics of protein unfolding and binding interactions. *Nat. Protoc.* **1**, 2527–2535 (2006).
30. V. Tugarinov, L. E. Kay, Ile, Leu, and Val methyl assignments of the 723-residue malate synthase G using a new labeling strategy and novel NMR methods. *J. Am. Chem. Soc.* **125**, 13868–13878 (2003).
31. P. Lundström, P. Vallurupalli, T. L. Religa, F. W. Dahlquist, L. E. Kay, A single-quantum methyl ^{13}C-relaxation dispersion experiment with improved sensitivity. *J. Biomol. NMR* **38**, 79–88 (2007).
32. T. Yuwen, P. Vallurupalli, L. E. Kay, Enhancing the sensitivity of CPMG relaxation dispersion to conformational exchange processes by multiple-quantum spectroscopy. *Angew. Chem., Int. Ed.* **55**, 11490–11494 (2016).
33. Z. Luz, S. Meiboom, Nuclear magnetic resonance study of the protolysis of trimethylammonium ion in aqueous solution—Order of the reaction with respect to solvent. *J. Chem. Phys.* **39**, 366–370 (1963).
34. S. Jo, T. Kim, V. G. Iyer, W. Im, CHARMM-GUI: A web-based graphical user interface for CHARMM. *J. Comput. Chem.* **29**, 1859–1865 (2008).
35. J. C. Phillips, R. Braun, W. Wang, J. Gumbart, E. Tajkhorshid, E. Villa, C. Chipot, R. D. Skeel, L. Kalé, K. Schulten, Scalable molecular dynamics with NAMD. *J. Comput. Chem.* **26**, 1781–1802 (2005).
36. R. B. Best, X. Zhu, J. Shim, P. E. M. Lopes, J. Mittal, M. Feig, A. D. MacKerell Jr., Optimization of the additive CHARMM all-atom protein force field targeting improved sampling of the backbone ϕ, ψ and side-chain χ₁ and χ₂ dihedral angles. *J. Chem. Theory Comput.* **8**, 3257–3273 (2012).

37. U. Essmann, L. Perera, M. L. Berkowitz, T. Darden, H. Lee, L. G. Pedersen, A smooth particle mesh Ewald method. *J. Chem. Phys.* **103**, 8577–8593 (1995).

38. J.-P. Ryckaert, G. Ciccotti, H. J. C. Berendsen, Numerical integration of the cartesian equations of motion of a system with constraints: molecular dynamics of *n*-alkanes. *J. Comput. Phys.* **23**, 327–341 (1977).

39. W. Humphrey, A. Dalke, K. Schulten, VMD: Visual molecular dynamics. *J. Mol. Graph.* **14**, 33–38 (1996).

40. A. A. Zamyatnin, Protein volume in solution. *Prog. Biophys. Mol. Biol.* **24**, 107–123 (1972).

Citation: Y. Toyama, K. Kontani, T. Katada, I. Shimada, Decreased conformational stability in the oncogenic N92I mutant of Ras-related C3 botulinum toxin substrate 1. *Sci. Adv.* **5**, eaax1595 (2019).